Two-Dimensional Design Strategy to Construct Smart Fluorescent Probes for the Precise Tracking of Senescence

Ying Gao,[a+] Yulu Hu,[a+] Qimeng Liu,[a+] Xiaokang Li,[b] Xinming Li,[b] Chu-Young Kim,[c] Tony D. James,[d] Jian Li,*[be] Xi Chen,*[a] and Yuan Guo*[a]

[a] Y. Gao,[+] Y. Hu,[+] Q. Liu,[+] Prof. X. Chen, Prof. Y. Guo
Key Laboratory of Synthetic and Natural Functional Molecule of the Ministry of Education, College of Chemistry and Materials Science, Northwest University, Xi'an, 710127, China
E-mail: guoyuan@nwu.edu.cn (Y. Guo); xchen@nwu.edu.cn (X. Chen)
[b] Dr. X. Li, Dr. X. Li (Xinming Li), Prof. J. Li
State Key Laboratory of Bioreactor Engineering, Shanghai Key Laboratory of New Drug Design, School of Pharmacy, East China University of Science and Technology, Shanghai, 200237, China
E-mail: jianli@ecust.edu.cn (J. Li)
[c] Prof. C.-Y. Kim
Department of Chemistry and Biochemistry, The University of Texas at El Paso, El Paso, 79968, United States
[d] Prof. T. D. James
Department of Chemistry, University of Bath, Bath, BA2 7AY, United Kingdom
[e] Prof. J. Li
Clinical Medicine Scientific and Technical Innovation Center, Shanghai Tenth People's Hospital, Tongji University School of Medicine, Shanghai, 200092, China
[+] These authors contributed equally.

Supporting information for this article is given via a link at the end of the document.

Abstract: The tracking of cellular senescence usually depends on the detection of senescence-associated β-galactosidase (SA-β-gal). Previous probes for SA-β-gal with this purpose only cover a single dimension: the accumulation of this enzyme in lysosomes. However, this is insufficient to determine the destiny of senescence because endogenous β-gal enriched in lysosomes is not only related to senescence, but also to some other physiological processes. To address this issue, we introduce our fluorescent probes including a second dimension: lysosomal pH, since de-acidification is a unique feature of the lysosomes in senescent cells. With this novel design, our probes achieved excellent discrimination of SA-β-gal from cancer-associated β-gal, which enables them to track cellular senescence as well as tissue aging more precisely. Our crystal structures of a model enzyme *E. coli* β-gal mutant (E537Q) complexed with each probe further revealed the structural basis for probe recognition.

Introduction

Cellular senescence is a permanent block to cell-cycle progression and caused by DNA damage, telomere shortening and dysfunction, oncogenic effects, and other types of cellular stress.[1] Although the main role of this process is to prevent abnormal cell proliferation, the chronic accumulation of senescent cells in tissues impairs organismal functions and exacerbates aging.[2] Tracking senescence by biomarkers and further precise interventions have been considered to be a promising approach to revert long-term degenerative changes and ameliorate aging-associated diseases.[2b,c,3] Secreted and/or intracellular proteins, such as γH2AX, p21, p16, IL-6, macroH2A, PPP1A, Smurf2, phosphorylated p38MAPK, and PGM have been used as biomarkers of cellular senescence and new candidates such as DEP1, NTAL, EBP50, VAMP3, ARMX3, STX4, LANCL1, B2MG, VPS26A and PLD3 have been proposed.[4] Senescence-associated β-galactosidase (SA-β-gal, as represented in Figure 1a), an endogenous lysosomal enzyme, is a potentially important aging biomarker when compared with the above protein markers.[5] The tracking of cellular senescence and whole tissue aging usually depends on the detection of the enzymatic activity of SA-β-gal.

Traditionally, a colorimetric assay for SA-β-gal is performed at pH 6 with fixed cells where hydrolysis of the substrate X-gal produces a blue color.[5] Nowadays fluorescent probes have been successfully applied to visualize cellular β-galactosidase (β-gal) with fast response and improved accuracy.[6] Such fluorescence assays are available to track the enzymatic activity of β-gal associated with ovarian cancer,[6b] vascular aging[6e] and the senescence of human diploid fibroblasts with high passage numbers.[6a] Endogenous β-gals enriched in these human cells, all originating from the gene of *GLB1* expressed in lysosomes, are not only related to senescence, but also to certain cancers (such as ovarian cancer) and some specific cell types (such as matured human mononuclear phagocytes and osteoclasts).[7] As a result, it is not sufficient to determine the destiny of senescence only by the feature of β-gal. The challenge then becomes how to differentiate SA-β-gal from other sources of endogenous β-gal such as ovarian cancer-associated β-gal. So far no specific probe has been developed for this purpose, which remains a gap in the field of aging research. Therefore, we introduce a novel concept of two-dimensional probes to overcome the above challenge. The initial detection of SA-β-gal relied on its hydrolyzing activity is defined as the first dimension. Then the second dimension is the microenvironment of this lysosomal enzyme, more specifically the pH within lysosomes, which can be indicated by the decline of vacuolar acidity discovered by Hughes and Gottschling during the early asymmetric divisions of a mother cell[8] and higher pH in lysosomes of aged animals reported by Liu *et al*.[9] In a normal state, the pH of lysosomes is acidic (4.0-6.5)[10] and its pH gradient is mainly generated by a V-type ATPase (V-ATPase) which drives protons to enter into the lysosome lumen by the

free energy of ATP hydrolysis (Figure 1a).[11] This process has been revealed to be important especially for cellular senescence and the late-onset neurodegenerative diseases.[11b] Our results indicate that the pH in lysosomes does increase with the progression of senescence, which is a specific characteristic distinct from that of cancer cells, and clearly demonstrate the value of our two-dimensional approach.

Herein, we report on the first generation of the above proposed two-dimensional probes **KSA01** and **KSA02** for the precise tracking of senescence (Figure 1b). They can operate sensitively in the first dimension through cleavage of the C–O glyosidic bond in the β configuration with β-gal to release the **KSAP1** and **KSAP2** fluorophores. Subsequently, these probes work in a second dimension by monitoring the changing lysosomal environment during aging, using the pH-dependent ratiometric fluorescence patterns of **KSAP1** and **KSAP2** which also match the pH windows of lysosomes. With this novel design, our probes achieved excellent discrimination of SA-β-gal from endogenous β-gal in ovarian cancer cells not associated with senescence, which enables them to specifically track cellular senescence as well as tissue aging. Notably, we demonstrated for the first time that both the endogenous SA-β-gal and the intrinsic lysosomal pH in living cells and in tissues increased with aging using a single dual-functional fluorescent probe. The application of a single probe prevents potential cross-talk by two probes working at the same time and facilitates more reliable analysis by self-calibration of two emission bands. We have further determined the crystal structures of both probes bound to the *E. coli* β-gal mutant (E537Q) respectively, which provides guidance for the structurally understanding of the recognition mechanism of these types of enzymes with such probes.

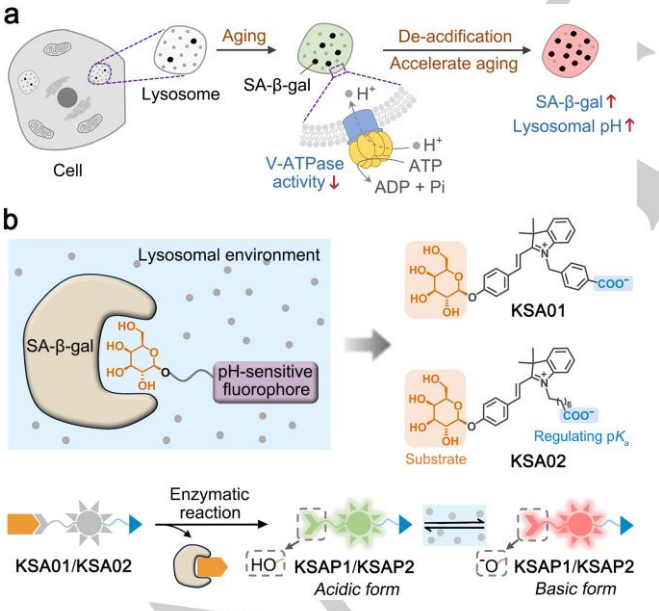

Figure 1. Design strategy. (a) Schematic illustration of age-related lysosomal changes. (b) Schematic illustration of the design concept (upper) and the proposed sensing mechanism (lower) for two-dimensional SA-β-gal fluorescent probes.

Results and Discussion

Design and synthesis of the two-dimensional fluorescent probes. In 2019, Hu et al. reported a β-gal probe **MC-βGal**, which can be hydrolyzed by β-gal and then release a pH sensitive merocyanine dye.[6p] Therefore, in order to obtain SA-β-gal probes sensitive to lysosomal pH, we developed two merocyanine-based fluorescent dyes **KSAP1** and **KSAP2** with the potential for detecting lysosomal pH. The two dyes differ from the simple merocyanine dye by Hu et al. in that their p*K*a values have been modified to coincide with the pH range of lysosomes through the introduction of carboxyl groups. The introduction of a fatty acid group to **KSAP2** results in a pK_a value of 6.2, which is higher than that of **KSAP1** (5.8) with an aromatic carboxylic acid group (Figure 2a and Figure S1b,d). The fluorescence spectra of the two dyes were measured in PBS buffers (100 mM) at the pH values ranging from 3.0 to 10.0. When the pH increased from 3.0 to 10.0, the fluorescence intensity at short wavelength (536 nm for **KSAP1** and 534 nm for **KSAP2**) gradually decreased and that of long wavelength (569 nm for **KSAP1** and 562 nm for **KSAP2**) increased (Figure S1a,c), indicating that the two dyes exhibit ratiometric response to pH changes. Then, a β-D-galactosyl group as the β-gal targeting and quenching group was attached to the dyes *via* a glyosidic bond, to create the final non-fluorescent two-dimensional probes **KSA01** and **KSA02** sensitive to both the endogenous SA-β-gal and the intrinsic lysosomal pH.

The sensing mechanism of KSA01 and KSA02. We propose the following molecular working mechanism for **KSA01** and **KSA02** (Figure 1b lower). In the first step, upon binding to β-gal, the glyosidic bond of our probes is cleaved to release the pH sensitive fluorescent dyes **KSAP1** or **KSAP2**. This was confirmed by mass spectrometry which indicated that after incubation of **KSA01** with *A. oryzae* or *E. coli* β-gal, peaks at m/z 398.1722 or 398.1735 appeared, corresponding to the mass of **KSAP1** (Figure S2a). Similar results were obtained for **KSA02** (Figure S2b). Afterwards, upon release, these two dyes exist mainly in the phenolic hydroxyl group form (“acidic form”) with weaker intramolecular charge transfer (ICT) effects and emit green fluorescence under an acidic lysosomal environment. However, under more basic lysosomal environment, they mainly exist in the phenolic anion form (“basic form”) with stronger ICT effects and emit red fluorescence. The normalized absorption and fluorescence spectra of **KSA01** and **KSA02** after incubation with *A. oryzae* β-gal at pH 4.0 or with *E. coli* β-gal at pH 7.4 overlapped with **KSAP1** and **KSAP2** at pH 4.0 or at pH 7.4 (Figure S3), presenting green and red fluorescence respectively, thus confirming this hypothesis. The above-mentioned unique two-dimensional sensing mechanisms enable our probes to recognize the lysosomal pH environment of this enzyme following the detection of β-gal.

***In vitro* testing of KSA01 and KSA02.** We used *A. oryzae* β-gal, which has optimum activity at pH of 4.0-5.0,[12] and *E. coli* β-gal, which has optimum activity at pH of 6.5-7.5 for *in vitro* studies.[13] Both probes showed minimum fluorescence in the absence of β-gal but produced a strong and pH dependent fluorescence when *A. oryzae* β-gal or *E. coli* β-gal were present (Figure S1e-h). Therefore, we selected the combination of *A. oryzae* β-gal and *E. coli* β-gal as a suitable *in vitro* model for the *in vitro* evaluation.

The absorption and fluorescence spectra of **KSA01** and **KSA02** were investigated in PBS buffer (100 mM, pH 4.0) at 37 °C before and after the addition of *A. oryzae* β-gal, respectively. The absorption spectra of **KSA01** and **KSA02** exhibited maximum absorption at 405 nm and 385 nm (Figure

S4a and Figure 2c). After adding *A. oryzae* β-gal, the maximum absorption of **KSA01** and **KSA02** shifted to 435 nm and 423 nm respectively in PBS buffer (Figure S4a and Figure 2c). The two probes displayed very low fluorescence in the absence of any β-gal but produced a strong green fluorescence signal upon the addition of *A. oryzae* β-gal, at 536 nm for **KSA01** and at 534 nm for **KSA02** (Figure S4b and Figure 2d). Furthermore, the fluorescence intensity exhibited excellent linear correlation with *A. oryzae* β-gal concentration (R^2 = 0.991 for **KSA01** and R^2 = 0.991 for **KSA02**) (Figure S4b and Figure 2d). The detection limits for **KSA01** and **KSA02** are 8.3×10^{-3} U/mL and 6.8×10^{-3} U/mL, respectively (IUPAC definition, LOD = 3σ/k). Our results demonstrate that at pH 4.0, the optimal pH for *A. oryzae* β-gal activity, **KSA01** and **KSA02** presented good optical responses to this enzyme. Then the selectivity and competition assays of **KSA01** and **KSA02** were evaluated after the addition of various potential interfering components including enzymes, amino acids and biomolecules in PBS buffer (100 mM, pH 4.0). Only *A. oryzae* β-gal produced an obvious "light-up" fluorescence signal (Figure S5a,c), indicating that both **KSA01** and **KSA02** exhibited high selectivity with minimal interference for detecting *A. oryzae* β-gal in complex systems. In addition, the kinetics for the two probes on this enzyme are different. Upon the introduction of *A. oryzae* β-gal, the fluorescence intensity increased gradually and reached a plateau within 13 min for **KSA01** and 9 min for **KSA02** (Figure S7a,c).

The same experiments were performed for **KSA01** and **KSA02** with *E. coli* β-gal in PBS buffer (100 mM, pH 7.4) at 37 °C and corresponding results were obtained (Figure S4c,d, Figure 2e,f, Figure S5b,d and Figure S7b,d). The detailed statistics were summarized in Table S1. These results indicate that **KSA01** and **KSA02** are not only able to respond to *E. coli* β-gal well, but also emit red fluorescence at the optimal pH of 7.4, which is different from the response with *A. oryzae* β-gal. Furthermore, we systematically investigated the fluorescence responses of the probes towards various concentrations of enzymes with different pH buffer solutions. The obtained three-dimensional representations more intuitively established the two-dimensional detection ability of our probes (Figure S4e and Figure 2b).

Crystal structures of *E. coli* β-gal in complex with KSA01 or KSA02. We generated a hydrolysis mutant of *E. coli* β-gal (E537Q) for crystallography studies of our probes. The **KSA01**-β-gal and **KSA02**-β-gal crystal structures were solved at the resolution of 2.70 Å and 2.67 Å respectively. Data collection and refinement statistics are summarized in Table S2. The two structures are highly similar (RMSD = 0.735 Å). **KSA01** forms hydrogen bonds with N102, D201, Y503, Q537 and H540 of *E. coli* β-gal mutant (E537Q), whereas **KSA02** forms hydrogen bonds with N102, D201, E461, M502, Q537, H540 and N604 (Figure 3a-d). For both **KSA01** and **KSA02**, the benzyl ring participates in a π-π stacking interaction with W999, and a likely magnesium and sodium ion are located within interaction distance (Figure 3a-d). Previous studies reported a "shallow" and a "deep" mode of substrate binding,[14] and these are also observed in our crystal structures (Figure S6b). **KSA01** adopts the "deep" binding mode, similar to how galactose binds to β-gal (PDB ID: 1JZ7). In contrast, **KSA02** adopts the "shallow" binding mode, similar to how **PNPG** binds to β-gal (PDB ID: 1JYW). It was previously observed that β-gal substrates bind in a "shallow" location near the entrance of the active site, while transition state analogues, intermediates, and the products penetrate 1–4 Å deeper into the pocket.[15] Another interesting observation is the contrasting conformation of the galactosyl ring. In **KSA02** the galactosyl ring adopts the "chair" conformation while in **KSA01** it adopts an intermediate conformation between "chair" and "boat". This is in agreement with the previous proposal that converting the galactosyl group to the boat conformation promotes hydrolysis by reducing steric clashes between the aglycon and the enzyme.[14]

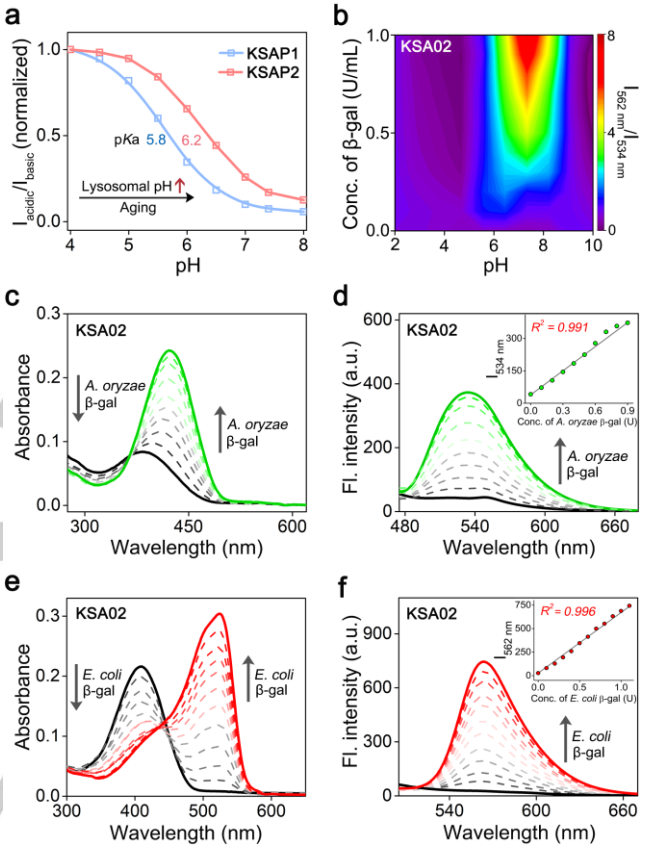

Figure 2. Spectral profiles. (a) Plots of I_{acidic}/I_{basic} versus the pH values in the range 4.0-8.0 for **KSAP1** ($I_{536\ nm}/I_{569\ nm}$) and **KSAP2** ($I_{534\ nm}/I_{562\ nm}$). (b) Three-dimensional representations of the fluorescence spectra of **KSA02** (10 μM) towards various concentrations of β-gal using different pH buffer solutions. Colour bars, the ratio of $I_{562\ nm}/I_{534\ nm}$. $I_{534\ nm}$ represents the fluorescence intensity at 534 nm upon adding different concentrations of *A. oryzae* β-gal (0-1.0 U/mL) in PBS buffers (100 mM) at different pH values (λ_{ex} = 460 nm, slit: 5 nm/10 nm); $I_{562\ nm}$ represents the fluorescence intensity at 562 nm upon adding different concentrations of *E. coli* β-gal (0-1.0 U/mL) in PBS buffers (100 mM) at different pH values (λ_{ex} = 490 nm, slit: 5 nm/10 nm). (c,d) Absorption (c) and fluorescence spectra (d) of **KSA02** (10 μM) upon adding different concentrations of *A. oryzae* β-gal (0-0.9 U/mL) in PBS buffer (100 mM, pH 4.0), respectively (λ_{ex} = 460 nm, slit: 5 nm/10 nm). Inset: a linear relationship between fluorescence intensity ($I_{534\ nm}$) and concentrations of *A. oryzae* β-gal (0-0.9 U/mL). (e,f) Absorption (e) and fluorescence (f) spectra of **KSA02** (10 μM) upon adding different concentrations of *E. coli* β-gal (0-1.1 U/mL) in PBS buffer (100 mM, pH 7.4), respectively (λ_{ex} = 490 nm, slit: 5 nm/10 nm). Inset: a linear relationship between fluorescence intensity ($I_{562\ nm}$) and concentrations of *E. coli* β-gal (0-1.1 U/mL).

With the guidance of the crystal structures of *E. coli* β-gal mutant (E537Q) complexed with fluorescent probes **KSA01** and **KSA02**, docking of the two probes to human β-gal were performed, respectively (Figure 3e,f). Similar to the *E. coli* β-gal mutant (E537Q) complexes, multiple hydrogen bonds form between the galactosyl group of the probes and human β-gal

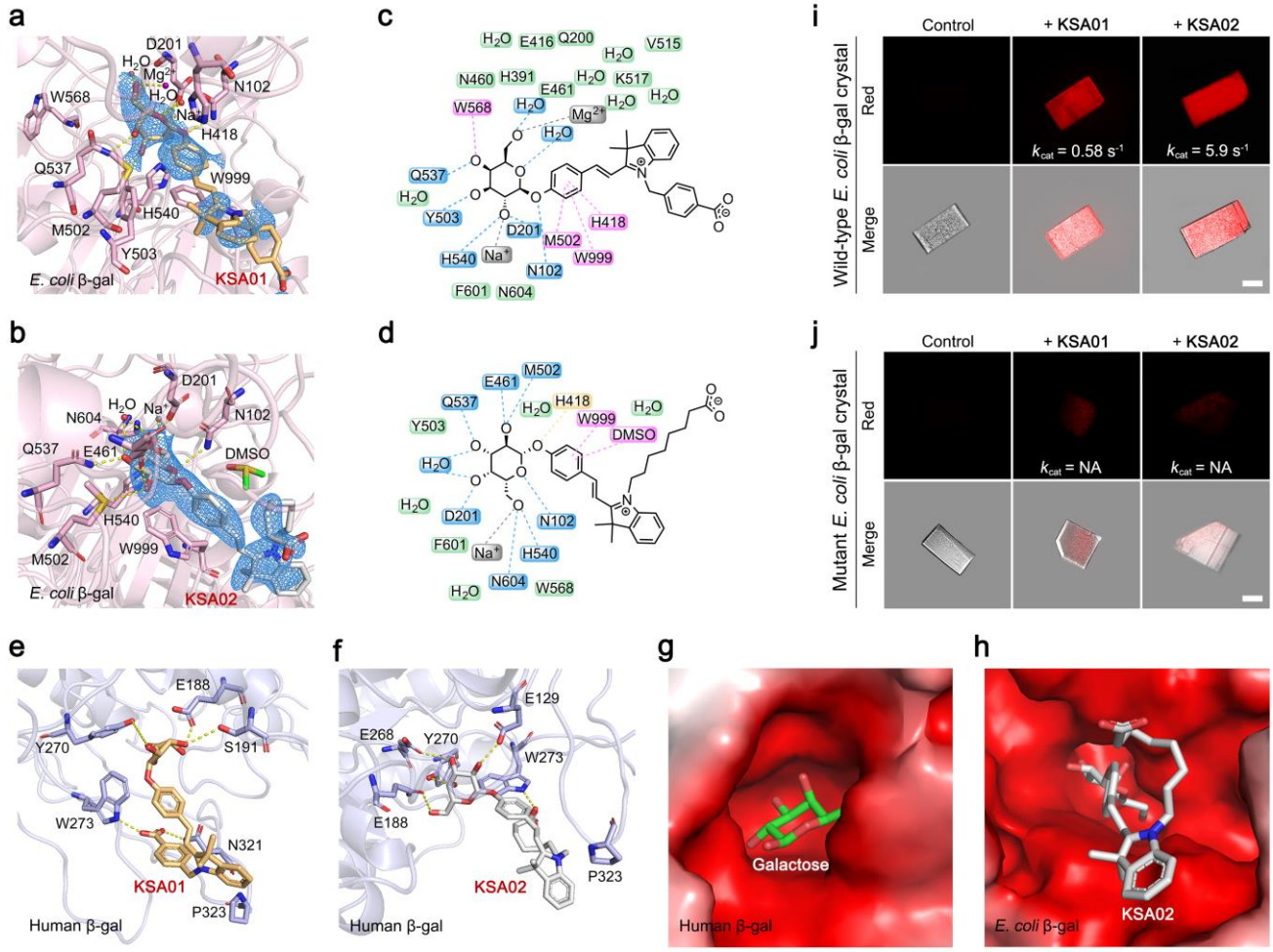

Figure 3. Structural determination of the interactions between β-gal and the probes. (a) Interactions between *E. coli* β-gal and the probe **KSA01** (PDB: 7BTK) and the electron density for **KSA01** in domain A (2Fo-2Fc map contoured at 1.0, blue mesh). (b) Interactions between *E. coli* β-gal and the probe **KSA02** (PDB: 7BRS) and the electron density for **KSA02** in domain A (2Fo-2Fc map contoured at 1.0, blue mesh). (c) Schematic diagram of *E. coli* β-gal-**KSA01** interactions shown in (a). (d) Schematic diagram of *E. coli* β-gal-**KSA02** interactions shown in (b). Hydrogen bonds, carbon hydrogen bonds, metal-acceptor and pi interaction are indicated as blue dashed lines, yellow dashed lines, grey dashed lines and purple dashed lines, respectively (c and d). (e) Interactions between human β-gal and the probe **KSA01** (docking). (f) Interactions between human β-gal and the probe **KSA02** (docking). Yellow dashed lines represent hydrogen bonds and interactions with metals (a, b, e and f). (g,h) Electrostatic surface potential of the substrate binding pocket in human β-gal with **Galactose** (g, PDB: 3THC) and in *E. coli* β-gal with **KSA02** (h, PDB: 7BRS). Negative electrostatic potential is presented in red while positive electrostatic potential is presented in blue (g and h). (i) Confocal images of crystals of the wildtype *E. coli* β-gal in complex with **KSA01** or **KSA02**. (j) Confocal images of crystals of the mutant *E. coli* β-gal in complex with **KSA01** or **KSA02**. NA, not available. Red channel, λ_{ex} = 488 nm, λ_{em} = 570-620 nm (i and j). Scale bars = 50 μm (i) and 100 μm (j). *E. coli* β-gal is shown as cartoon (a and b) in pink while human β-gal is shown as cartoon in blue (e and f). **KSA01**, **KSA02** and **Galactose** are shown as sticks with carbon atoms colored in orange, grey and green, respectively. Oxygen and nitrogen atoms are shown in red and blue, respectively. Sodium ions are presented as grey nb_spheres while magnesium ions are presented as purple nb_spheres (a and b).

(Figure 3e,f). There is also a weak π-π stacking interaction between W273 and the benzyl ring of **KSA01** or **KSA02**. The electrostatic potentials of substrate binding pockets in *E. coli* β-gal mutant (E537Q) and human β-gal are very alike: both are highly negative charged (Figure 3g,h). These features indicate that human β-gal might recognize **KSA01** and **KSA02** through similar interaction networks. In addition, our *in vivo* assays showed that **KSA01** and **KSA02** emitted fluorescence when tested with different human cell lines enriched with endogenous β-gal, which demonstrates that these probes are also substrates for human β-gal. Therefore, these structures can be used as backbones for future human β-gal fluorescent probe design.

Meanwhile, wild-type *E. coli* β-gal crystals were obtained successfully under slightly different conditions (please refer to the Supporting Information). Confocal imaging was applied to detect the fluorescence produced by wild-type *E. coli* β-gal crystals with probes **KSA01** and **KSA02** and *E. coli* β-gal mutant (E537Q) as control. After soaking wild-type *E. coli* β-gal crystals with probes **KSA01** and **KSA02**, a significant fluorescence enhancement was observed (Figure 3i). However, the *E. coli* β-gal mutant (E537Q) did not cause any fluorescence enhancement with the two probes (Figure 3j), which indicates that this mutant is inactive while the wild-type *E. coli* β-gal is highly active even in the crystalline state. The catalytic rate (k_{cat}) of the wild-type *E. coli* β-gal for **KSA01** and **KSA02** were measured separately to be 0.58 s^{-1} and 5.9 s^{-1} (Figure 3i and Figure S7e,f) while for the mutant *E. coli* β-gal the results were not possible (NA) (Figure 3j) since it displayed almost no hydrolytic activity, indicating that the catalytic function of this mutant was successfully repressed.

Cell imaging. Inspired by the results of *in vitro* experiments, we evaluated **KSA01** and **KSA02** in living cells. First, the cytotoxicity of the two probes towards various living cells was evaluated using a CCK-8 assay (Figure S8). Both the probes

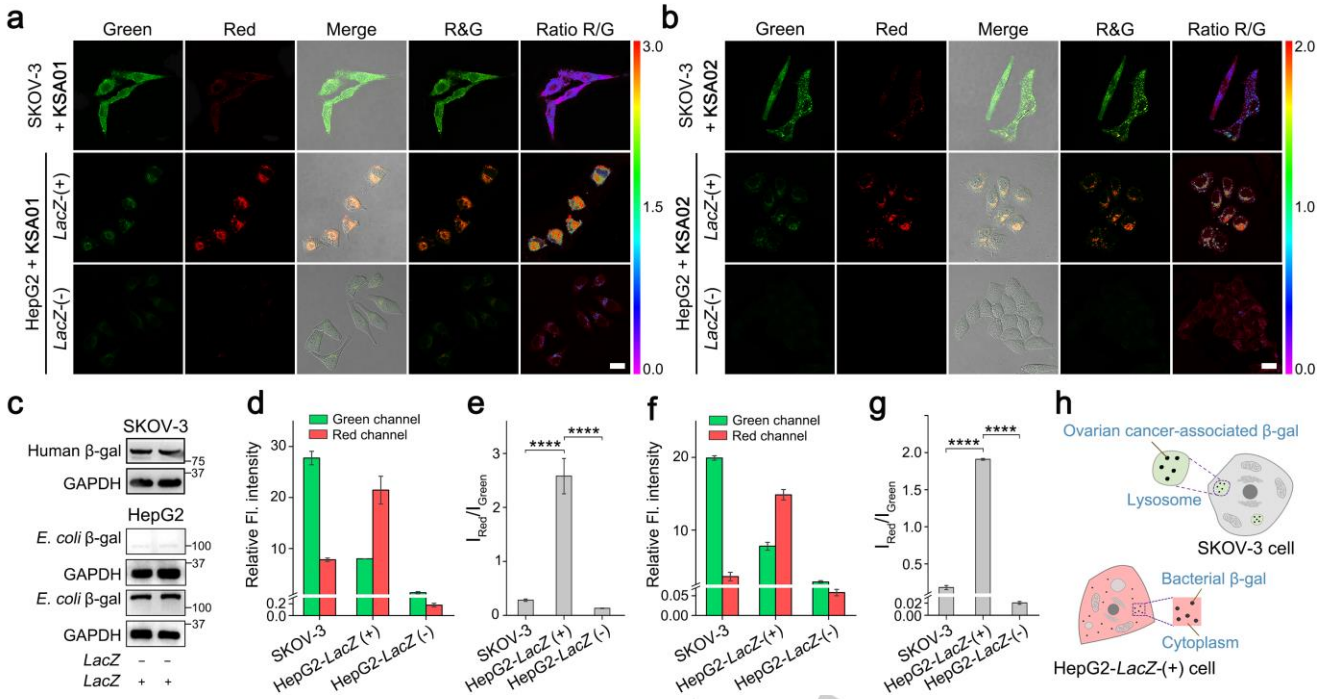

Figure 4. Imaging of endogenous ovarian cancer-associated β-gal and exogenous bacterial β-gal in living cells. (a,b) Confocal images of SKOV-3 cells, HepG2-*LacZ*-(-) cells and HepG2-*LacZ*-(+) cells stained with **KSA01** (300 μM, 30 min) and **KSA02** (300 μM, 30 min) on a Nikon A1 laser-scanning confocal microscope, respectively. (c) Western blot analysis to determine the expression of human β-gal in SKOV-3 cells and the expression of *E. coli* β-gal in HepG2-*LacZ*(+) cells. GAPDH was used as an internal reference. (d,f) Quantification of relative fluorescence intensity in the green channel and red channel of groups (a) and (b), respectively. (e,g) Quantification of fluorescence intensity ratios (I_{Red}/I_{Green}) in groups (a) and (b), respectively. (h) Schematic representation of the distribution of ovarian cancer-associated β-gal in SKOV-3 cell and bacterial β-gal in HepG2-*LacZ*-(+) cell. Green channel, λ_{ex} = 405 nm, λ_{em} = 500-550 nm; red channel, λ_{ex} = 488 nm, λ_{em} = 570-620 nm. Scale bars = 20 μm (a and b). Error bars represent the standard deviation (± S.D.) with n = 3. Significant differences (****P < 0.0001) are analyzed with two-sided Student's *t*-test.

exhibited low cytotoxicity and good biocompatibility with living cells. Next, both probes were used for fluorescence imaging of endogenous lysosomal β-gal in living cells (Figure 4 and Figure S10). Human ovarian cancer cell lines (SKOV-3 and OVCAR-3 cells) which also overexpress human endogenous β-gal[6b,6d,7a] in lysosomes were selected as the cell models whose β-gal are associated with ovarian cancer. In addition, the overexpression of human β-gal in SKOV-3 cells was confirmed by a western blot assay (Figure 4c). In contrast, human non-small lung cancer cells (A549) and normal human liver cells (HL-7702), both of which do not overexpress this enzyme were chosen as control cell models. As expected, A549 cells and HL-7702 cells exhibited weak fluorescence signals in both the green and red channels (Figure S9 and Figure S10), while SKOV-3 and OVCAR-3 cells exhibited significantly higher fluorescence, with higher intensity in the green channel compared to the red channel (Figure 4a,b,d-g and Figure S10). Since the lysosomes in cancer cells have higher metabolic capacity and lower pH,[16] the two probes mostly emitted the green fluorescence signal corresponding to the "acidic form" of each probe in the lysosomes of ovarian cancer cells, as represented in Figure 4h. Confocal images of SKOV-3 cells treated with LysoTracker Deep Red, a lysosome-specific NIR probe, showed good agreement with images obtained with **KSA01** and **KSA02**, with Pearson's correlation coefficient (PCC) values of 0.87 and 0.90, respectively (Figure S11a). In order to confirm that fluorescence intensity changes in the green and red channels are associated with the pH values, the plasmid pLVX-Puro-*LacZ* with the *LacZ* gene for *E. coli* β-gal was transfected into human liver cancer cells (HepG2) to construct a *LacZ*-(+) cell line with increased *E. coli* β-gal expression which was clearly verified by a western blot assay (Figure 4c). *E. coli* β-gal, unlike mammalian β-gal, is located in the cytoplasm which has a neutral pH, as represented in Figure 4h.[4c] Treating *LacZ*-(+) HepG2 cells with **KSA01** and **KSA02** resulted in significant fluorescence enhancements in both the green and red channels (Figure 4a,b,d-g), but more so in the red channel which corresponds to the predominating "basic form". Additionally, the distribution of extralysosomal exogenous *E. coli* β-gal was further confirmed by the poor overlap between the fluorescence in the red channel of **KSA01** and **KSA02** and that in the NIR channel of LysoTracker Deep Red in *LacZ*-(+) HepG2 cells, with low PCC values of 0.53 and 0.39, respectively (Figure S11b). These results indicated that our probes were able to detect both endogenous and exogenous β-gal in living cells, and they could also report on the microenvironmental pH of β-gal.

Then **KSA01** and **KSA02** were used to simultaneously monitor the changes in SA-β-gal activity and lysosomal pH during senescence. Human lung fibroblastic cells (MRC-5) were cultured from passage 21 (P21) to passage 24 (P24) to obtain replicative senescent cells at different senescent stages,[17] which were previously verified using X-gal staining (Figure 5b). MRC-5 cells (P21) incubated with **KSA01** exhibited weak fluorescence in the green channel and negligible fluorescence in the red channel (Figure 5a,c). With increasing passage number (P22-P24), the fluorescence intensity of the MRC-5 cells gradually increased in both channels, with the intensity from the red channel increasing more rapidly (Figure 5a,c). At the same time, the sum of the fluorescence intensity (I_{Red} + I_{Green}) and the ratio of fluorescence intensity (I_{Red}/I_{Green}) were also amplified

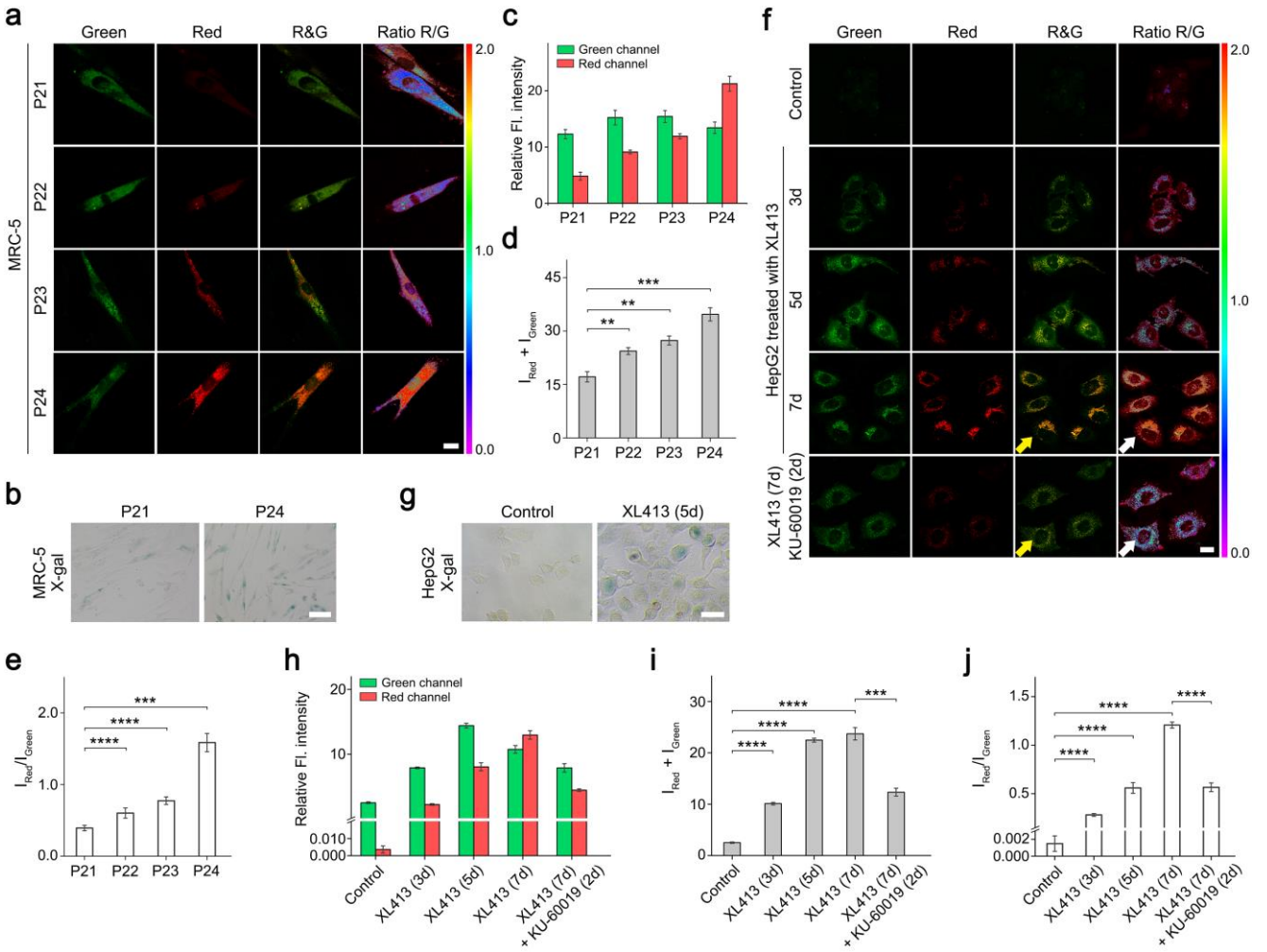

Figure 5. Imaging of SA-β-gal in living cells. (a) Confocal images of MRC-5 cells at different stages from passage 21 (P21) to passage 24 (P24) incubated with **KSA01** (300 μM, 30 min) on an Olympus FV1000 laser-scanning confocal microscope. (b) Images after staining for SA-β-gal activity at different stages of MRC-5 cells by a conventional X-gal chemical assay. (c) Quantification of relative fluorescence intensity in the green channel and red channel of group (a). (d) Quantification of fluorescence intensity sums (I_{Red} + I_{Green}) in group (a). (e) Quantification of fluorescence intensity ratios (I_{Red}/I_{Green}) in group (a). (f) Row 1-4: confocal images of HepG2 cells treated without or with XL413 (5 μM) for different times (3 days, 5 days and 7 days) and then incubated with **KSA02** (300 μM, 30 min) on a Nikon A1 laser-scanning confocal microscope. Row 5: confocal images of HepG2 cells treated with XL413 (5 μM, 7 days), followed by treatment with KU-60019 (0.5 μM, 2 days) and then incubated with **KSA02** (300 μM, 30 min) on a Nikon A1 laser-scanning confocal microscope. (g) Images after staining for SA-β-gal activity with HepG2 cells and XL413 treated HepG2 cells by a conventional X-gal chemical assay. (h) Quantification of relative fluorescence intensity in the green channel and red channel of group (f). (i) Quantification of fluorescence intensity sums (I_{Red} + I_{Green}) in group (f). (j) Quantification of fluorescence intensity ratios (I_{Red}/I_{Green}) in group (f). Green channel, λ_{ex} = 405 nm, λ_{em} = 500-550 nm; red channel, λ_{ex} = 488 nm, λ_{em} = 570-620 nm. Scale bars = 20 μm (a and f), 50 μm (b and g). Error bars represent the standard deviation (± S.D.) with n = 3. Significant differences (***P* < 0.01, ****P* < 0.001, *****P* < 0.0001) are analyzed with two-sided Student's *t*-test.

(Figure 5d,e), indicating that during senescence the SA-β-gal content and lysosomal pH both increased gradually in MRC-5 cells. In order to confirm this result, we investigated the fluorescence imaging of **KSA02** in HL-7702 cells treated with doxorubicin (DOX) which has been shown to induce senescence by damaging DNA (Figure S12).[4c] A western blot assay was preformed to confirm the protein overexpression of senescence-associated human β-gal in DOX-treated HL-7702 cells (Figure 6d-f). Compared to untreated HL-7702 cells, the fluorescence signals in the green and red channels were enhanced in the DOX-treated senescent HL-7702 cells after staining with **KSA02** (Figure S12). Furthermore, the fluorescence intensity observed for the red channel was greater than that for the green channel.

Next, we treated senescent HepG2 cells with our probes to evaluate changes in SA-β-gal levels and the lysosomal pH. HepG2 cells were treated with XL413 which induces senescence by inhibiting the function of the DNA replication kinase CDC7.[18] The senescence state of XL413-treated HepG2 cells was verified using X-gal staining (Figure 5g). Then HepG2 cells treated by XL413 for different length of time or not treated with this inhibitor were imaged after the addition of **KSA02**. The untreated cells displayed negligible fluorescence in both the green and red channels, while the fluorescence intensity gradually increased in both the channels for the XL413-treated cells over time (Figure 5f,h). Moreover, with increasing treatment time, the enhancement of the green channel gradually deceased while that of the red channel continued to increase, which could be quantified by determining total fluorescence intensity (I_{Red} + I_{Green}) and the fluorescence intensity ratio (I_{Red}/I_{Green}) (Figure 5i,j). Our data indicated that the SA-β-gal level as well as the lysosomal pH of cancer cells gradually increased during senescence. Moreover, the pH values of lysosomes in HepG2 cells with senescence were measured by using a ratiometric lysosomal pH dye (LysoSensor Yellow/Blue DND-160) (Figure

S13a,b) and the results further demonstrated that the pH values of lysosomes increased with senescence. **KSA01** was also used for the same imaging experiments (Figure S14) and the results are consistent with those for **KSA02** (Figure 5f). However, under the same conditions, the fluorescence intensity ratio (I_{Red}/I_{Green}) for **KSA01** was higher than that for **KSA02**, which can be explained by the lower pK_a value of **KSAP1** than that of **KSAP2**. For senescent HepG2 cells undergoing XL413 treatment for 3 days, **KSA02** output in the red channel was negligible resulting in a reduced I_{Red}/I_{Green} ratio. In comparison, **KSA01** exhibited better performance than **KSA02** with an increased I_{Red}/I_{Green} ratio and a detectable red fluorescence signal. Similarly, these cancer cells treated with XL413 for 5-7 days were not severely senescent and still exhibited low lysosomal pH, making **KSA01** a better probe to study the progression of senescence. However, for the more severely senescent HL-7702 cells (healthy cells) treated with DOX and exhibiting higher lysosomal pH, **KSA02** was chosen instead of **KSA01** for imaging due to the significant red channel emission of **KSA01** resulting in an excessive I_{Red}/I_{Green} ratio. Therefore, in order to obtain appropriate imaging results, the I_{Red}/I_{Green} ratio should not be too low or too high. As such, we propose that for the early stages of senescence when the lysosomal pH is low, **KSA01** should be used, but for later stages with higher lysosomal pH, **KSA02** is more suitable for use. In addition, Hep3B cells were treated with LY3177833, a senescence inducer similar to XL413,[18] to obtain additional senescent model cells, which was then verified by using a western blot assay (Figure S15i). Then both **KSA01** and **KSA02** were applied to study the senescence of these cells and the results were consistent with those of the senescent HepG2 cells (Figure S15), which further confirmed our statements.

Based on the above confocal imaging findings, it can be seen that the images obtained by the probes in senescent cells are significantly different from those in SKOV-3 cells. In order to display this difference more intuitively, we compared the images of senescent HL-7702 cells enriched by SA-β-gal and SKOV-3 cells overexpressing ovarian cancer-associated β-gal using **KSA02**, as shown in Figure 6a and Figure S12. **KSA02** mostly exhibited red fluorescence signal in senescent HL-7702 cells, while it mainly produced a green fluorescence signal in SKOV-3 cells, which indicated that the probe is capable of discriminating SA-β-gal from ovarian cancer-associated β-gal. We further compared the protein expression levels of human β-gal and another senescence marker γH2AX in the two types of cells. The results supported the overexpression of human β-gal in SKOV-3 cells (Figure 4c and Figure 6d-f) and the overexpression of both human β-gal and γH2AX in DOX-treated HL-7702 cells (Figure 6d-f), from which it can be concluded that the β-gal in SKOV-3 cells is not associated with senescence. In addition, the pH values in the lysosomes of SKOV-3 and senescent HL-7702 cells were accurately measured to be 4.27 and 5.43, respectively (Figure 6b and Figure S13c-e), which further confirmed that the lysosomal pH in senescent cells is higher than that in cancer cells. These results ensure the reliability of our strategy based on the detection of endogenous β-gal activity in combination with the monitoring of lysosomal microenvironmental pH.

So far, very few anti-aging drugs have been approved for clinical trials, mainly because of a lack of consensus drug evaluation tools based on aging biomarkers.[19] KU-60019, as a representative ataxia-telangiectasia mutated (ATM) kinase specific inhibitor, has been found to exhibit senescence alleviation by regulating the V-ATPase activity and maintaining lysosomal pH.[20] **KSA02** was used to evaluate the anti-aging function of KU-60019 in living cells. Compared with the senescent HepG2 cells (undergoing XL413 treatment for 7 days), the fluorescence intensity sum ($I_{Red} + I_{Green}$) and the fluorescence intensity ratio (I_{Red}/I_{Green}) of the same cells treated with KU-60019 decreased significantly (Figure 5f,h-j), indicating that the level of SA-β-gal decreased and the function of lysosomes was repaired in senescent cells treated with this anti-aging drug. Therefore, our two-dimensional probe is a promising tool to evaluate these kinds of drugs.

In summary, HL-7702, HepG2 and Hep3B cells treated with drugs capable of inducing cell senescence and MRC-5 cells with high passages provided different types of senescent cell models with overexpression of SA-β-gal, including healthy cells and cancer cells. Untreated A549 and HL-7702 cells with low expression of β-gal were used as negative control groups. SKOV-3 and OVCAR-3 cells overexpressing ovarian cancer-associated β-gal and *LacZ*-(+) HepG2 cells overexpressing *E. coli* β-gal were used as β-gal cell models not associated with senescence. The foregoing experimental results in these cell models demonstrate that our two-dimensional probes can precisely track senescence at the cellular level *via* the detection of both β-gal and lysosomal microenvironmental pH.

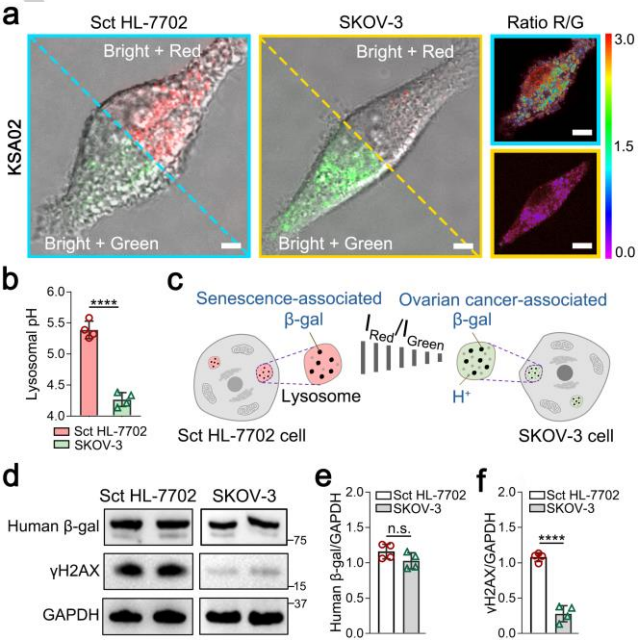

Figure 6. Comparison of imaging between SA-β-gal and ovarian cancer-associated β-gal in living cells. (a) Confocal images of senescent (sct) HL-7702 cells and SKOV-3 cells stained with **KSA02** (300 μM, 30 min). Sct HL-7702 cells model was obtained by treating HL-7702 cells with DOX for 1 day. Green channel, λ_{ex} = 405 nm, λ_{em} = 500-550 nm; red channel, λ_{ex} = 488 nm, λ_{em} = 570-620 nm. Scale bars = 5 μm (a, column 1 and column 2) and 10 μm (a, column 3). (b) Quantification of lysosomal pH values in sct HL-7702 cells and SKOV-3 cells using a ratiometric lysosomal pH dye (LysoSensor Yellow/Blue DND-160). (c) Schematic representation of the distributions of SA-β-gal in DOX-induced sct HL-7702 cells and ovarian cancer-associated β-gal in SKOV-3 cells. (d) Western blot analysis to determine human β-gal and γH2AX expressions in sct HL-7702 cells and SKOV-3 cells. GAPDH was used as an internal reference. Quantifications are shown in (e) and (f). Error bars represent the standard deviation (± S.D.) with n = 4. Significant differences (n.s., not significant, ****P < 0.0001) are analyzed with two-sided Student's t-test.

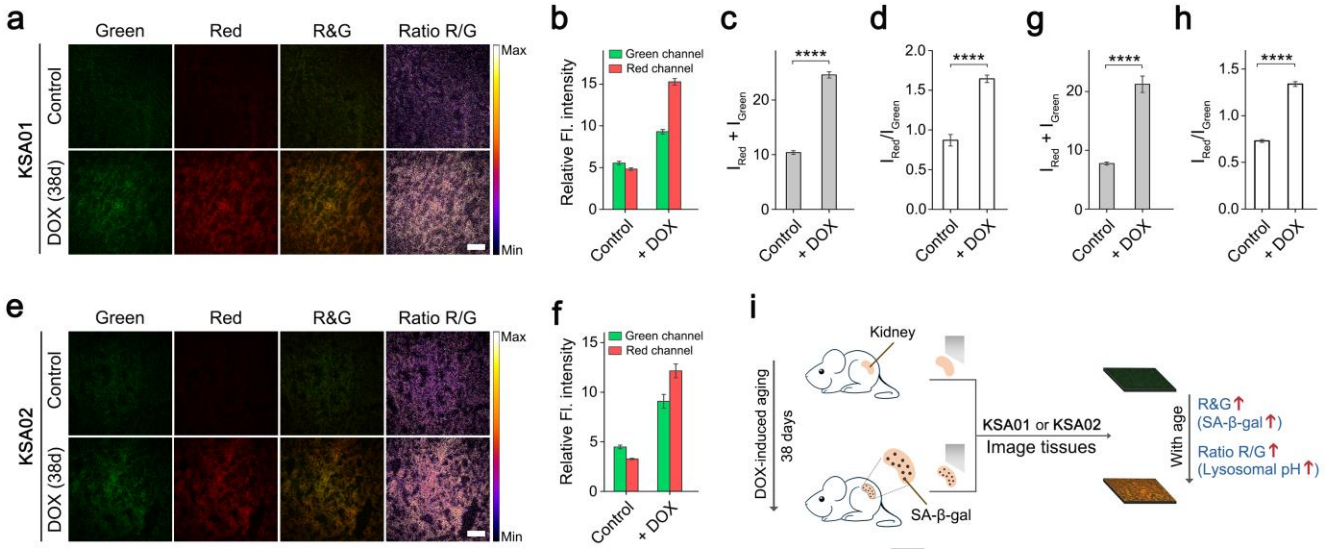

Figure 7. Imaging of SA-β-gal in kidney tissues. (a,e) Representative fluorescence images of treated without or with DOX (38 days) C57BL/6J male mice kidney sections incubated with **KSA01** (300 μM) and **KSA02** (300 μM) on a Leica TCS SP8 laser-scanning confocal microscope, respectively. (b,f) Quantification of relative fluorescence intensity in the green channel and red channel of groups (a) and (e), respectively. (c,g) Quantification of fluorescence intensity sums (I_{Red} + I_{Green}) in groups (a) and (e), respectively. (d,h) Quantification of fluorescence intensity ratios (I_{Red}/I_{Green}) in groups (a) and (e), respectively. (i) Schematic representation of kidney tissues imaging in young and aging mice using **KSA01** and **KSA02**. Green channel, λ_{ex} = 405 nm, λ_{em} = 500-550 nm; red channel, λ_{ex} = 488 nm, λ_{em} = 570-650 nm. Scale bars = 100 μm (a and e). Error bars represent the standard deviation (± S.D.) with n = 3. Significant differences (****P < 0.0001) are analyzed with two-sided Student's *t*-test.

Tissue imaging. The kidneys are one of the organs most prone to senescence[21] and the capability of **KSA01** and **KSA02** to visualize SA-β-gal in kidney tissue exhibiting different degrees of aging was investigated. The kidney tissue sections from 1-, 13- and 23-month-old C57BL/6J male mice were treated with **KSA01** and **KSA02**, respectively. Confocal imaging indicated that the fluorescence intensity of the green and red channels increased with age and the enhancement for the green channel is lower than that for the red channel, which could be quantified as the sum of fluorescence intensity (I_{Red} + I_{Green}) and the fluorescence intensity ratio (I_{Red}/I_{Green}) (Figure S16). In addition, **KSA01** and **KSA02** were used to image SA-β-gal in the kidney tissue of DOX-induced aged C57BL/6J male mice. Compared with the control group, DOX-induced aged kidney tissue exhibited a remarkable enhancement of fluorescence intensity in both green and red channels, both the sum of fluorescence intensity (I_{Red} + I_{Green}) and the fluorescence intensity ratio (I_{Red}/I_{Green}) increased (Figure 7). These results indicated that the level of SA-β-gal and the pH of the microenvironment in kidney tissue increased with age.

Based on all our above experimental results, we now wish to explain why SA-β-gal is associated with aging and speculate the mechanism as follows. In young lysosomes, the pH is about 4.5, which is the optimal working condition for human β-gal. As cellular division increases, lysosomal deacidification occurs, and thus the environmental pH is no longer optimal for the enzyme. In order to maintain normal working efficiency, more β-gal is produced and accumulates in lysosomes. This feedback mechanism is reminiscent of the *LacZ* operon regulation in *E. coli*: when there is sufficient substrate (allolactose), the substrate binds to the repressor so that the production of β-gal is implemented and thus there are more enzymes to consume the substrate. As a feedback, when there is less substrate, the repressor binds to the operator and stops the transcription of the gene for β-gal.

Conclusion

In summary, we have proposed a two-dimensional design strategy to construct smart fluorescent probes for the precise tracking of senescence through the comprehensive analysis of SA-β-gal activity as well as its local microenvironment simultaneously. Then the first generation of the above proposed two-dimensional probes **KSA01** and **KSA02** have been developed herein. The crystal structures of *E. coli* β-gal mutant (E537Q) complexed with each probe and the modeled structures of human β-gal in complex with our probes revealed the structural basis for probe recognition. Our two-dimensional design enabled the probes to track senescence more precisely in living cells in addition to characterize tissue aging more accurately. As expected, the imaging results showed that our probes mostly emitted red fluorescence signal in senescent cells, while in ovarian cancer cells a green fluorescence signal was observed. As far as we know, this is the first example of a small-molecular fluorescent probe which is capable of discriminating SA-β-gal from ovarian cancer-associated β-gal. Furthermore, using our smart two-dimensional probe, the anti-aging function of KU-60019 was convincingly evaluated in living cells. Therefore, the unique two-dimensional visualization approach will pave the way to specifically illustrate the process of aging and facilitate the development of anti-aging drugs.

Acknowledgements

We appreciate the gift of the plasmid containing the sumo-tag from Prof. Shu Quan. We thank the staffs from BL17B/BL18U1 beamline of National Facility for Protein Science in Shanghai (NFPS) at Shanghai Synchrotron Radiation Facility, for assistance during data collection. We thank the experimental facility and the technical services provided by the Synchrotron

Radiation Protein Crystallography Facility of the Taiwan Core Facility Program for Biotechnology, and the Taiwan Synchrotron Radiation Research Center. We gratefully acknowledge the financial support from the NSF of China (22037002, 21977082, 21472148 and 21807088), the Natural Science Basic Research Plan for Distinguished Young Scholars in Shaanxi Province of China (2020JC-38) and the Technology Plan Project of Xi'an (GXYD18.1). TDJ wishes to thank the Royal Society for a Wolfson Research Merit Award. YG thanks the University of Orleans in France for the invited professor position.

Keywords: senescence • β-galactosidase • lysosomal pH • fluorescent probes • bioimaging

[1] a) M. Collado, M. A. Blasco, M. Serrano, *Cell* **2007**, *130*, 223-233; b) M. A. Blasco, *Nat. Chem. Biol.* **2007**, *3*, 640-649; c) S. Khosla, J. N. Farr, T. Tchkonia, J. L. Kirkland, *Nat. Rev. Endocrinol.* **2020**, *16*, 263-275.

[2] a) D. Muñoz-Espin, M. Serrano, *Nat. Rev. Mol. Cell Biol.* **2014**, *15*, 482−496; b) B. G. Childs, M. Gluscevic, D. J. Baker, R.-M. Laberge, D. Marquess, J. Dananberg, J. M. V. Deursen, *Nat. Rev. Drug Discov.* **2017**, *16*, 718-735; c) Y. Cai, H. Zhou, Y. Zhu, Q. Sun, Y. Ji, A. Xue, Y. Wang, W. Chen, X. Yu, L. Wang, H. Chen, C. Li, T. Luo, H. Deng, *Cell Res.* **2020**, *30*, 574-589.

[3] S. He, N. E. Sharpless, *Cell* **2017**, *169*, 1000-1011.

[4] a) M. Althubiti, L. Lezina, S. Carrera, R. Jukes-Jones, S. M. Giblett, A. Antonov, N. Barlev, G. S. Saldanha, C. A. Pritchard, K. Cain, S. Macip, *Cell Death Dis.* **2014**, *5*, 1528; b) A. Hernandez-Segura, J. Nehme, M. Demaria, *Trends Cell Biol.* **2018**, *28*, 436-453; c) B. Lozano-Torres, A. Estepa-Fernández, M. Rovira, M. Orzáez, M. Serran, R. Martínez-Máñez, F. Sancenón, *Nat. Rev. Chem.* **2019**, *3*, 426-441.

[5] G. P. Dimri, X. Lee, G. Basile, M. Acosta, G. Scott, C. Roskelley, E. E. Medrano, M. Linskensi, I. Rubelj, O. Pereir-Smithiia, M. Peacocke, J. Campisi, *Proc. Natl. Acad. Sci. U. S. A.* **1995**, *92*, 9363-9367.

[6] a) H. W. Lee, C. H. Heo, D. Sen, H.-O. Byun, I. H. Kwak, G. Yoon, H. M. Kim, *Anal. Chem.* **2014**, *86*, 10001-10005; b) D. Asanuma, M. Sakabe, M. Kamiya, K. Yamamoto, J. Hiratake, M. Ogawa, N. Kosaka, P. L. Choyke, T. Nagano, H. Kobayashi, Y. Urano, *Nat. Commun.* **2015**, *6*, 6463; c) K. Gu, Y. Xu, H. Li, Z. Guo, S. Zhu, S. Zhu, P. Shi, T. D. James, H. Tian, W.-H. Zhu, *J. Am. Chem. Soc.* **2016**, *138*, 5334-5340; d) B. Lozano-Torres, I. Galiana, M. Rovira, E. Garrido, S. Chaib, A. Bernardos, D. Muñoz-Espín, M. Serrano, R. Martínez-Máñez, F. Sancenón, *J. Am. Chem. Soc.* **2017**, *139*, 8808-8811; e) E.-J. Kim, A. Podder, M. Maiti, J. M. Lee, B. G. Chung, S. Bhuniy, *Sens. Actuators B* **2018**, *274*, 194-200; f) H.-W. Liu, L. Chen, C. Xu, Z. Li, H. Zhang, X.-B. Zhang, W. Tan, *Chem. Soc. Rev.* **2018**, *47*, 7140-7180; g) H. Ito, Y. Kawamata, M. Kamiya, K. Tsuda-Sakurai, S. Tanaka, T. Ueno, T. Komatsu, K. Hanaoka, S. Okabe, M. Miura, Y. Urano, *Angew. Chem. Int. Ed.* **2018**, *57*, 15702-15706; h) X. Zhen, J. Zhang, J. Huang, C. Xie, Q. Miao, K. Pu, *Angew. Chem. Int. Ed.* **2018**, *57*, 7804-7808; i) M. Chiba, M. Kamiya, K. Tsuda-Sakurai, Y. Fujisawa, H. Kosakamoto, R. Kojima, M. Miura, Y. Urano, *ACS Cent. Sci.* **2019**, *5*, 1676-1681; j) X. Li, W. Qiu, J. Li, X. Chen, Y. Hu, Y. Gao, D. Shi, X. Li, H. Lin, Z. Hu, G. Dong, C. Sheng, B. Jiang, C. Xia, C.-Y. Kim, Y. Guo, J. Li, *Chem. Sci.* **2020**, *11*, 7292-7301; k) Y. Zhang, C. Yan, C. Wang, Z. Guo, X. Liu, W.-H. Zhu, *Angew. Chem. Int. Ed.* **2020**, *59*, 2-10; l) X. Chai, H.-H. Han, A. C. Sedgwick, N. Li, Y. Zang, T. D. James, J. Zhang, X.-L. Hu, Y. Yu, Y. Li, Y. Wang, J. Li, X.-P. He, H. Tian, *J. Am. Chem. Soc.* **2020**, *142*, 18005-18013; m) B. Lozano-Torres, J. F. Blandez, I. Galiana, A. García-Fernández, M. Alfonso, M. D. Marcos, M. Orzáez, F. Sancenón, R. Martínez-Máñez, *Angew. Chem. Int. Ed.* **2020**, *59*, 15152-15156; n) Y. Wang, J. Liu, X. Ma, C. Cui, P. R. Deenik, P. K. P. Henderson, A. L. Sigler, L. Cui, *Sci. Rep.* **2019**, *9*: 2102; o) J. Zhang, C. Li, C. Dutta, M. Fang, S. Zhang, A. Tiwari, T. Werner, F.-T. Luo, H. Liu, *Anal. Chim. Acta* **2017**, *968*, 97-104; p) X. Zhao, W. Yang, S. Fan, Y. Zhou, H. Sheng, Y. Cao, Y. Hu, *J. Lumin.* **2019**, *205*, 310-317.

[7] a) S. K. Chatterjee, M. Bhattacharya, J. J. Barlow, *Cancer Res.* **1979**, *39*, 1943-1951; b) I. Bursuker, J. M. Rhodes, R. Goldman, *J. Cell Physiol.* **1982**, *112*, 385-390; c) H.-G. Kopp, A. T. Hooper, S. V. Shmelkov, S. Rafii, *Histol. Histopathol.* **2007**, *22*, 971-976.

[8] A. L. Hughes, D. E. Gottschling, *Nature* **2012**, *492*, 261-265.

[9] J. Liu, W. Lu, D. Reigada, J. Nguyen, A. M. Laties, C. H. Mitchell, *Invest. Ophthalmol. Vis. Sci.* **2008**, *49*, 772-780.

[10] a) M. H. Lee, J. H. Han, J. H. Lee, N. Park, R. Kumar, C. Kang, J. S. Kim, *Angew. Chem. Int. Ed.* **2013**, *52*, 6206-6209; b) X. Chen, Z. Chen, B. Hu, P. Cai, S. Wang, S. Xiao, Y.-L. Wu, X. Chen, *Small* **2018**, *14*, 1703164.

[11] a) S. Ohkuma, Y. Moriyama, T. Takano, *Proc. Natl. Acad. Sci. U. S. A.* **1982**, *79*, 2758-2762; b) D. J. Colacurcio, R. A. Nixon, *Ageing Res. Rev.* **2016**, *32*, 75-88; c) M. B. Bagh, S. Peng, G. Chandra, Z. Zhang, S. P. Singh, N. Pattabiraman, A. Liu, A. B. Mukherjee, *Nat. Commun*. **2017**, *8*, 14612.

[12] M. J. Bailey, M. Linko, *J. Biotechnol.* **1990**, *16*, 57-66.

[13] G. R. Craven, E. Steers, C. B. Anfinsen, *J. Biol. Chem.* **1965**, *240*, 2468-2477.

[14] D. H. Juers, T. D. Heightman, A. Vasella, J. D. McCarter, L. Mackenzie, S. G. Withers, B. W. Matthews, *Biochemistry* **2001**, *40*, 14781-14794.

[15] B. W. Matthews, *C. R. Biol.* **2005**, *328*, 549-556.

[16] Z. Xue, H. Zhao, J. Liu, J. Han, S. Han, *ACS Sens.* **2017**, *2*, 436-442.

[17] G. Hewitt, D. Jurk, F. D. M. Marques, C. Correia-melo, T. Hardy, A. Gackowska, R. Anderson, M. Taschuk, J. Mann, J. F. Passos, *Nat. Commun.* **2012**, *3*, 708.

[18] C. Wang, S. Vegna, H. Jin, B. Benedict, C. Lieftink, C. Ramirez, R. L. Oliveira, B. Morris, J. Gadiot, W. Wang, A. D. Chatinier, L. Wang, D. Gao, B. Evers, G. Jin, Z. Xue, A. Schepers, F. Jochems, A. M. Sanchez, S. Mainardi, H. T. Riele, R. L. Beijersbergen, W. Qin, L. Akkari, R. Bernards, *Nature* **2019**, *574*, 268-272.

[19] A. Zhavoronkov, *Science* **2020**, *368*, 595.

[20] a) H. T. Kang, J. T. Park, K. Choi, Y. Kim, H. J. C. Choi, C. W. Jung, Y.-S. Lee, S. C. Park, *Nat. Chem. Biol.* **2017**, *13*, 616-623; b) J. T. Park, Y.-S. Lee, K. A. Cho, S. C. Park, *Ageing Res. Rev.* **2018**, *47*, 176-182.

[21] Y. Zhang, A. Unnikrishnan, S. S. Deepa, Y. Liu, Y. Li, Y. Ikeno, D. Sosnowska, H. V. Remmen, A. Richardson, *Redox Biol.* **2017**, *11*, 30-37.

Entry for the Table of Contents

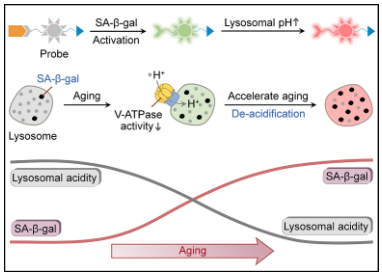

Here we report a two-dimensional design strategy to construct smart fluorescent probes for the precise tracking of senescence. Our approach relies on the detection of senescence-associated β-galactosidase activity in combination with the monitoring of lysosomal microenvironmental pH since de-acidification is a unique feature of the lysosomes in senescent cells.